Rainfall estimation from satellite passive microwave observations in the range 89 GHz to 190 GHz

E. Di Tomaso,[1] F. Romano,[1] and V. Cuomo[1]

[1] The aim of the present work is to improve the current state of rainfall estimation by proposing a procedure based entirely on the observations made by the US Advanced Microwave Sounding Unit/B (AMSU/B) on board the National Oceanic and Atmospheric Administration (NOAA) satellites. The procedure does not require the integration of additional sensors which could deteriorate the overall spatial and temporal resolution. It exploits both the radiometric observations made at 89 and 150 GHz (window channels) and the ones made in the 183 GHz water vapor band (opaque channels). In particular, the differences between the measurements of some of the AMSU/B channels are analyzed through radiative transfer simulations for the estimation of precipitation over both land and water surfaces and are related to rain rate values in different atmospheric scenarios. The algorithm estimates exhibit a very good agreement with ground-based (both radar and rain gauge) observations in the detection of rainfall and a reasonably good estimation of rain rate values. The probability of detection of precipitation is 75% and 90% for rain rates greater than 1 mm/h and 5 mm/h, respectively. Furthermore, due to the use of both window and opaque channels, the proposed procedure is able to retrieve light rain and not to misidentify snow-covered surfaces as rain.

Citation: Di Tomaso, E., F. Romano, and V. Cuomo (2009), Rainfall estimation from satellite passive microwave observations in the range 89 GHz to 190 GHz, *J. Geophys. Res.*, *114*, D18203, doi:10.1029/2009JD011746.

1. Introduction

[2] The accurate estimation of rainfall is crucial for many applications, both for short-term assessment and for long-term monitoring. In particular, nowcasting techniques rely on the integration of instantaneous retrieval of precipitation into data assimilation systems. Moreover, the recent decades have seen a considerable increase of extreme events which has accentuated the significance of rainfall remote sensing as a means of monitoring environmental hazards. Satellites outperform other instruments like ground radars and rain gauges in the observation of meteorological events as they ensure a global coverage of the Earth. Satellite retrieval methods use observations at visible, infrared and microwave (MW) frequencies. Among them, the microwave techniques provide the most direct observation of precipitation as microwave radiation is less affected by cloud droplets and interacts with precipitation-sized hydrometeors.

[3] The present work involves the use of radiometric sounding at passive MW frequencies (in the range 89 to 190 GHz) for the development of a precipitation algorithm which blends the physical observations with some prior knowledge of the nature of precipitation events. The radiation measured by microwave instruments is given in terms of brightness temperature (TB). There are two physical phenomena that have been exploited in the literature for rainfall retrieval at microwaves frequencies, namely emission and scattering. The first is observed mainly at low frequencies and the rainfall retrieval is based on the assumption of a relationship between the optical depth associated with the emitting raindrops and the rain at the surface. In particular, over ocean the low emissivity of the surface has allowed scientists to utilize emission by rain droplets to retrieve rainfall: over a cold background the emission effect leads to an increase of the brightness temperatures. Over land, the situation is more complex because emission by raindrops is viewed against a highly varying and highly emissive background. Instead, when considering higher frequencies (greater than 40 GHz) and heavy rain, the emission signal is too weak. Radiation emitted by rain is scattered downward by the overlying layer of ice particles, as the hydrometeor particle size is comparable to the wavelength of the radiation. As a consequence of the scattering effect, a decrease in brightness temperature is observed, which can be exploited assuming a relationship between ice in clouds and rain on the surface. This effect is less evident on certain types of precipitation, commonly nimbostratus clouds over ocean, with little or no ice layer. At present over ocean both emission and scattering have been used while over land only scattering is exploited.

[4] Different MW instruments have been used in the last few decades for rainfall remote sensing, among them there are the Tropical Rainfall Measuring Mission (TRMM) Microwave Imager, the Special Sensor Microwave Imager (SSM/I), the Advanced Microwave Scanning Radiometer

---

[1]Istituto di Metodologie per l'Analisi Ambientale, Consiglio Nazionale delle Ricerche, Tito Scalo, Italy.

(AMSR). The most recent operational or research algorithms [*Chen and Staelin*, 2003; *Ferraro et al.*, 2005] for rainfall retrieval utilize the US Advanced Microwave Sounding Unit (AMSU) on board the National Oceanic and Atmospheric Administration (NOAA) satellites. AMSU comprises two units, namely AMSU/A and AMSU/B together covering the frequency range 23 to 190 GHz. Most, if not all, retrieval algorithms based on AMSU/B utilize also the additional lower frequencies of AMSU/A despite its quite coarse spatial resolution (50 km at nadir). In the present study only AMSU/B observations will be used. Other instruments like SSM/I on board the DMSP (Defense Meteorological Satellites Program) series are equipped with lower frequency channels than AMSU/B sensitive to both emission and scattering, and are hence favored in detecting the emission signature over ocean [*Kummerow et al.*, 2001]. On the other hand, using AMSU/B offers several advantages. Foremost among them is the good spatial resolution (16 km at nadir), which is often an issue for MW instruments. Considering that there are three NOAA POES satellites spaced approximately four hour apart, also its temporal resolution is quite good. Furthermore, both NOAA N-18 and the MetOp-A satellites carry on board MHS (Microwave Humidity Sounder), an instrument with features very similar to AMSU/B, also operating in the 89 to 190 GHz range. The integration of the two instruments on all the five platforms can provide quite a good number of samples for daily precipitation products. Furthermore, it has been shown that AMSU/B high frequencies are more sensitive to smaller particles aiding retrievals of light rain over land [*Qiu et al.*, 2005] and help to detect solid precipitation [*Kongoli et al.*, 2003]. Weakness of AMSU/B is the cross-scan characteristic of the instrument: each scan produces observations of different footprint size due to different viewing angles from nadir, unlike conical scanning instruments such as SSM/I. Recently *Vila et al.* [2007] have worked out a correction for AMSU/B-derived rain rates depending on the viewing angle.

[5] The AMSU/B retrieval algorithms existing in the literature can be characterized according to the type of channels, window or opaque, they use. The characteristics of AMSU/B channels are described in more detail in section 2.1. The two window channels at 89 and 150 GHz are utilized in the NESDIS operational algorithms [*Ferraro et al.*, 2005] for global precipitation applications. The rain rate algorithm is based on the initial work of *Grody* [1991]. A parameter called scattering index is utilized to estimate the ice water path (IWP), whose relationship with rain rate is empirically tuned to coincident radars or physical tuned from cloud model simulations. The scattering index is utilized also by the precipitation cloud product of the EUMESAT Nowcasting Satellite Application Facility [*Bennartz et al.*, 2002]. In the NESDIS algorithms the rain rate is computed based on the IWP using different coefficients according to the type of precipitation system. A convective index is used to discriminate different type of precipitation systems into convective or moderate/low precipitation. The definition of convective index is based on the relative differences of the three AMSU/B opaque channel observations.

[6] The work by *Chen and Staelin* [2003] and *Staelin and Chen* [2000] utilizes only opaque channels of both AMSU/A

and /B in the oxygen and water vapor band, respectively. Their algorithm relies on the precipitation regions identified by the condition $TB_{183\pm7GHz} < 260$ K. A neural network is used to represent the nonlinear relation between microwave radiances and precipitation. The neural network relies on an extensive training set in order to generalize to new unseen cases, and depends heavily on the radar set used in training. Also in this case the precipitation signature is due to scattering, as the frequencies are too high and the scattering dominates the emission signal.

[7] More recently, blending techniques based on both infrared and microwave observations have been developed [*Joyce et al.*, 2004] to estimate rainfall at a global scale. Infrared instruments on board geostationary satellites are used to improve the temporal resolution of polar-orbiting microwave instruments.

2. Data and Instruments

[8] In this section some technical characteristics of AMSU/B are described together with some details on the ground-based instruments utilized in this work: the UK NIMROD radar network and the ARM Surface Meteorology Station.

2.1. AMSU/B

[9] AMSU/B is a cross-track, line scanning microwave radiometer measuring radiances in five channels in the frequency range 89 to 190 GHz. The center frequencies for the five channels are 89 GHz, 150 GHz, 183 ± 1 GHz, 183 ± 3 GHz, and 183 ± 7 GHz. The relative brightness temperatures are indicated in the paper as TB_f, where f is the channel center frequency. AMSU/B provides measurements of radiation from a number of different layers of the atmosphere. The lowest frequency channels (at 89 and 150 GHz) are able to measure the radiance up to the surface of the Earth and hence are characterized as window channels. The highest three channels are instead defined as opaque channels as they detect radiances at frequencies close to the water vapor absorption line at 183.31 GHz. AMSU/B observes the Earth scanning circa ±50 degrees across nadir and has an antenna beam width of 1.1 degrees. This gives a resolution of 16 Km at nadir and at a nominal altitude of 850 km, and 90 consecutive fields of view (FOVs) per scan. Further details on scan parameters and other instruments features can be found in the NOAA KLM user's guide [*NCDC/NOAA*, 2008]. AMSU/B is a water vapor sounder built with the aim to obtain global data on humidity profiles. Though it was not designed for rainfall retrieval, many studies prove that it is useful for this purpose. AMSU/B works in conjunction with AMSU/A, a 15 channel temperature sounder radiometer also on board NOAA satellites. At the time of writing, there are three operational NOAA POES satellite, namely N-15, N-16 and N-17, spaced approximately four hour apart and carrying the AMSU/B instrument. The AAPP6 code [*UK Met Office*, 2008a] is used to process the AMSU/B measurements.

2.2. NIMROD Radar Network

[10] Radar rain products from the UK NIMROD network are available from the British Atmospheric Data Centre [*UK Met Office*, 2008b] at a time resolution of 15 minutes and a spatial resolution of 5 km. They are based on the analysis of
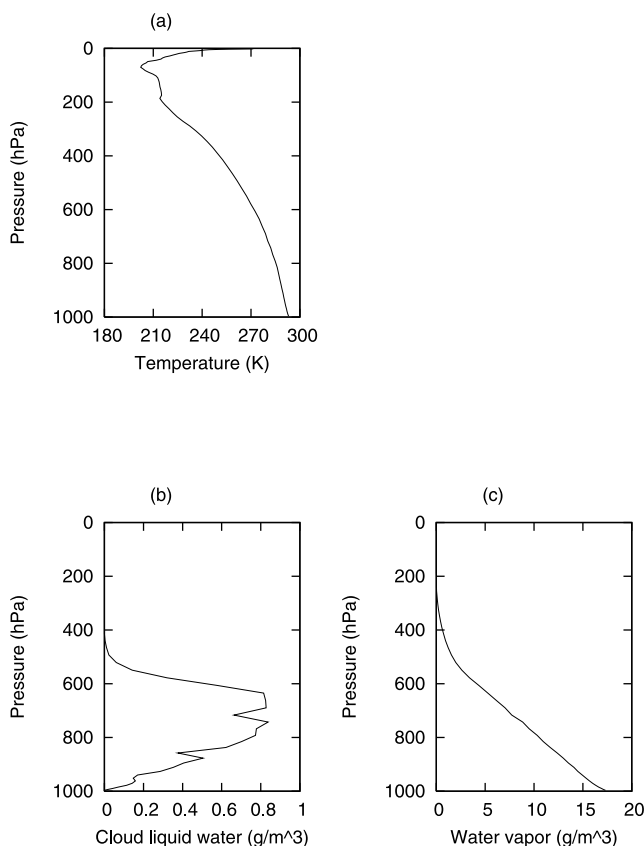
Figure 1. A profile of (a) atmospheric temperature, (b) cloud liquid water, and (c) water vapor from the diverse profile data set from the ECMWF 91-level short-range forecasts.

measurements from a network on C-band rainfall radars. The radar rain rate products are colocated with the AMSU/B FOVs so that each FOV has a corresponding radar-derived rainfall value. Only FOVs completely clear or fully covered by radar rain pixels are considered in the validation stage and only radar pixels with rain rates less than 150 mm/h. This is done in order to minimize sources of errors of radar-derived rain rates. Radar rain rates are in fact prone to errors, the most common sources of errors being ground clutter, radar beam filling, and a non accurate Z-R relationship [*Rico-Ramirez et al.*, 2007]. Since the AMSU/B FOV are larger than the radar pixels, high radar rain rates are generally averaged with lower rain rates in the colocation procedure. This is a general sampling problem associated with wide microwave fields of view.

2.3. ARM Surface Meteorology Station Rain Gauges

[11] The Surface Meteorology Station (SMET) is one of the Atmospheric Radiation Measurement (ARM) instruments on the island of Nauru, in the tropical western Pacific. The SMET station consists of a set of in situ sensors including an optical rain gauge. The rain gauge detects scintillation of an infrared beam caused by liquid water in the path. The voltage signal is then converted to a rain rate. The continuous measurements are sampled once a second and then averaged over each minute. The average point value of a minute interval is colocated with the AMSU/B

FOV overpassing the surface station in the same time interval.

3. Rainfall Estimation Procedure

[12] The following section introduces a novel rain rate retrieval procedure. The procedure is based on radiative transfer simulations at AMSU/B frequencies and on a number of real measurements. The radiative transfer simulation results are presented in section 3.1, and on the basis of these results, an algorithm for precipitation estimation at microwave frequencies (PEMW) is proposed in section 3.2. The PEMW algorithm is tested in section 4.

3.1. Radiative Transfer Simulations

[13] In order to study the effect of precipitation on the radiometric measurements, synthetic data are obtained by radiative transfer code simulations. For this purpose, the microwave radiative transfer program TBSCAT by *Rosenkranz* [2002] is utilized. TBSCAT computes top-of-atmosphere microwave brightness temperatures for an atmosphere defined by a given profile which describes, as function of pressure, the temperature, the water vapor density, the nonprecipitating cloud-liquid water density, and densities of four types of precipitation (rain, snow, graupel, and ice). A set of profiles from the European Centre for Medium-Range Weather Forecasts (ECMWF) is considered for the simulations, more specifically, the diverse profile data set from the ECMWF 91-level short-range forecasts [*UK Met Office*, 2008c]. This data set is available from the Satellite Application Facility for Numerical Weather Prediction (NWP SAF) and samples in turn, the atmospheric temperature, water vapor, ozone, cloud condensate and precipitation simulated by the ECMWF system. Figure 1 illustrates an example of one of the profiles used for the simulations, where atmospheric temperature, water vapor and cloud liquid water are function of pressure. The Marshall-Palmer distribution has been selected to represent the hydrometeor size distribution so that, given the rain rate value, the hydrometeor effective radii and their size distribution can be provided to the simulation software. Precipitation is set to occur up to circa 12 km and is liquid for temperatures greater than 273.15 K, and ice for colder temperatures. The refraction index is assigned a value from 0 to 0.3 for profiles over land surface, and from 0.4 to 0.6 for profiles over water surface. The channel brightness temperatures are computed from the single frequency TBSCAT output taking into account the different channel characteristics: the center frequency of the channels, the number of passbands and the bandwidth per passband. The ozone profile has not been taken into account as it was found that the additional ozone absorption would not affect the simulated results in the microwave domains considered.

[14] Typically, in case of rain, TB_{150GHz} registers a colder temperature than TB_{89GHz}, as observed in the work of R. Aschbrenner et al. (Development and intercomparison of AMSU rain rate algorithms, paper presented at 13th AMS Conference on Satellite Meteorology and Oceanography, Norfolk, VA, 19 September, 2004). However, in the case of light rain over ocean the warm emission signal caused by rainfall over the cold surface at 89 GHz is still too weak to overcome the emission sensed at 150 GHz. Also at the higher AMSU/B frequencies, the channels respond differ-
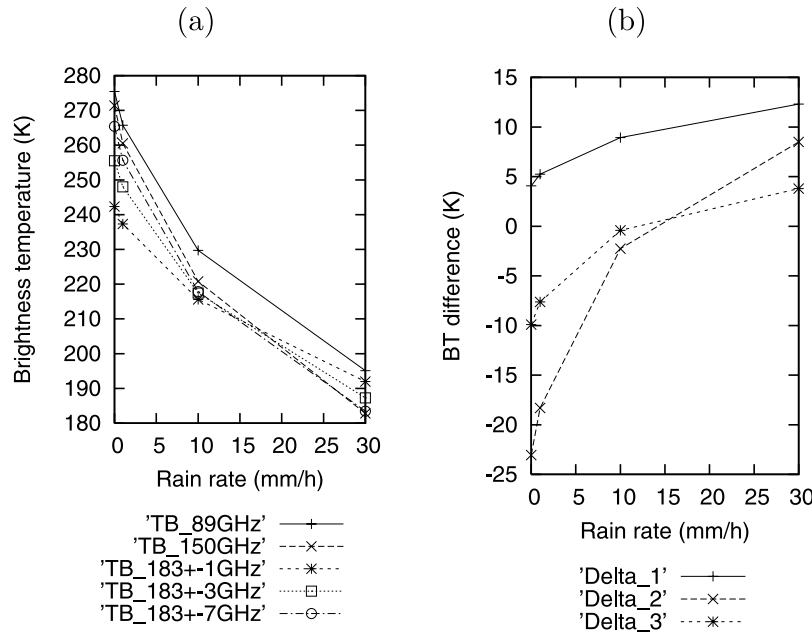
(a)   (b)

Figure 2. (a) AMSU/B brightness temperatures and (b) the differences Δ_1, Δ_2 and Δ_3 at different rain rate values.

ently in the presence of precipitation than in clear scenes. Typically, $TB_{183\pm7\,GHz}$ registers a stronger depression than the other two opaque channels. Hence the difference between brightness temperatures can provide a useful insight into the rate of precipitation. In particular, three differences are considered as follows:

$$\Delta_1 = TB_{89\,GHz} - TB_{150\,GHz}$$
$$\Delta_2 = TB_{183\pm1\,GHz} - TB_{183\pm7\,GHz}$$
$$\Delta_3 = TB_{183\pm3\,GHz} - TB_{183\pm7\,GHz}. \qquad (1)$$

[15] Figure 2 illustrates the simulated brightness temperatures at AMSU/B frequencies and their differences at different rain rate values for the profile of Figure 1. The behavior of the three above differences at varying rain rates is studied in a wide number of atmospheric/surface scenarios. At this stage only relatively small viewing angles are considered. Nevertheless, the same study can be applied also to large angles of view.

[16] The above study is used to fit an extensive set of regression curves between the brightness temperature differences Δ_i, for i = 1, 2, 3, and rain rate rr in various atmospheric and surface conditions, which forms the basis for the algorithm introduced in the following section. The synthetic data are utilized to study the variability of the coefficients for the above regression curves, taking into account also extreme scenarios, in order derive a domain (i.e., a minimum and maximum value) for each of these coefficients. The results are verified using a number of real AMSU/B measurements corresponding to rain rate values from the NIMROD radar product described in section 2.2. The ranges of values that these coefficients can assume are used in the rain rate retrieval algorithm of the next section.

3.2. Algorithm for Precipitation Estimation at Microwave Frequencies (PEMW)

[17] From the previous section it emerged that the differences between the observed AMSU/B brightness temper-

atures can provide useful information on the amount of precipitation. A single regression between one of the difference Δ_i and the amount of precipitation could potentially be enough to infer the rain rate. On the other hand, the determination of the regression coefficients for a general retrieval is not an easy task to accomplish as those coefficients need to be tuned for every specific atmospheric and surface scenario. For this reason a procedure is built that is able to select automatically the appropriate scenario and hence the suitable coefficients which fit a model between the observations and rain rate. A given curve $f(rr, \Delta_i | \theta_{i_1}, \ldots, \theta_{i_j}, \ldots, \theta_{i_c}) = 0$ is assumed to model the relationship between Δ_i and rr for i = 1, 2, 3, where θ_{i_j} for j = 1, ..., c are the coefficients for that curve. A table of possible values for θ_{i_j} is built, where each tuple $\Theta_k = \{\theta_{1_1}, \ldots, \theta_{1_c}, \ldots, \theta_{3_1}, \ldots, \theta_{3_c}\}$ for k = 1, ..., s is assumed to correspond to a possible atmospheric/surface scenario. The coefficient table is derived by the analysis of radiative code simulations, as explained in the previous section. In more detail, the coefficient domains are converted to discrete ones selecting a certain number of equispaced values over the continuous space. The combinations of the discrete values selected are taken as tuples Θ_k of the coefficient table. Given the five AMSU/B observations of a certain FOV, and the above assumption and table, the precipitation algorithm PEMW consists of the following steps:

[18] 1. Transformation of variables from the five observed brightness temperatures to the three differences Δ_1, Δ_2, Δ_3 as in equation (1).

[19] 2. Estimation of three rain rate values rr_{1_k}, rr_{2_k} and rr_{3_k} given Δ_1, Δ_2, Δ_3 and for each possible scenario k (i.e., tuple of coefficients θ_{i_j} present in the given table) as follows:

$$f(rr_{1_k}, \Delta_1, \Theta_k) = 0$$
$$f(rr_{2_k}, \Delta_2, \Theta_k) = 0$$
$$f(rr_{3_k}, \Delta_3, \Theta_k) = 0, \quad k = 1, \ldots, s. \qquad (2)$$

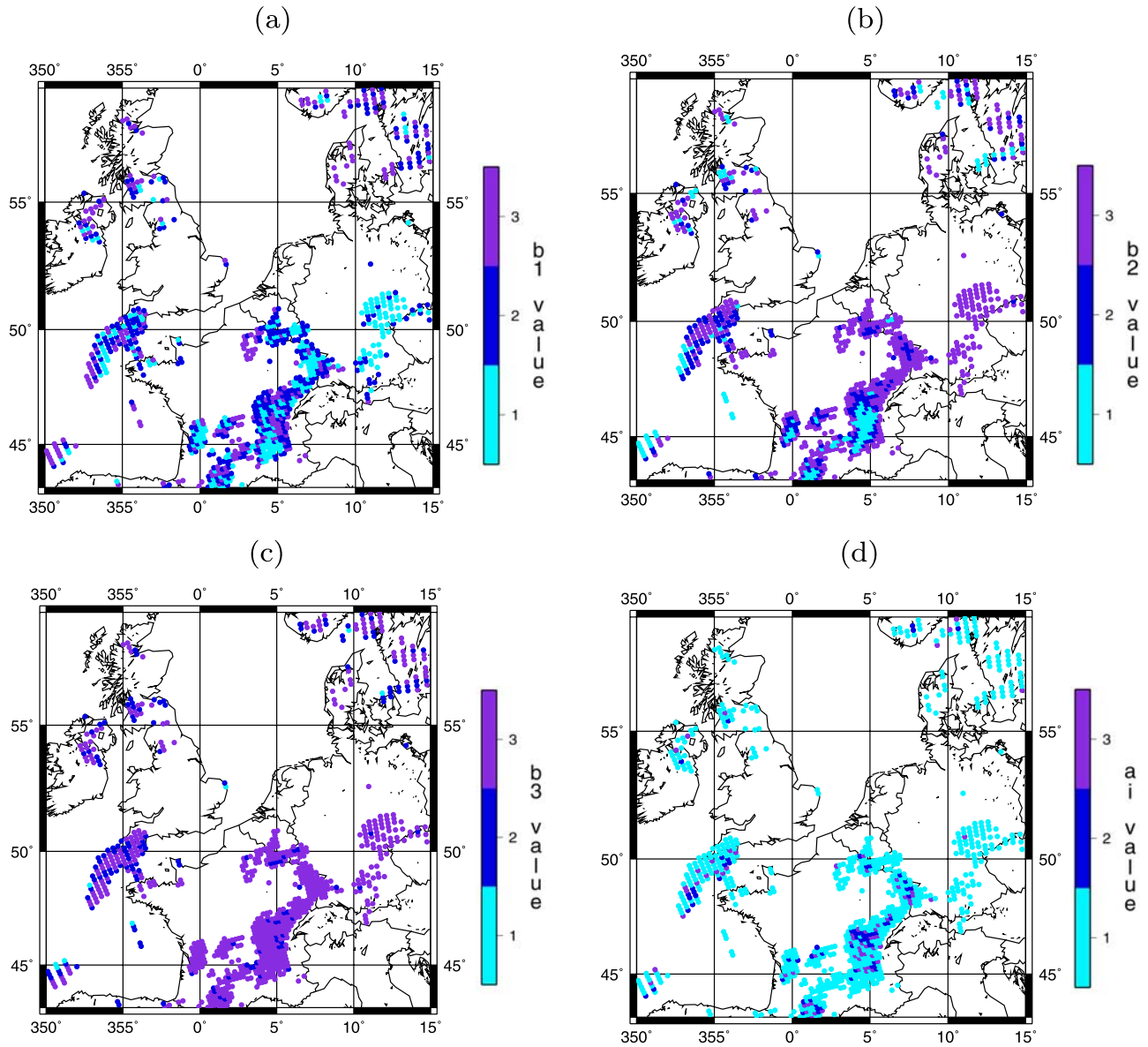**Figure 3.** The scenarios selected by the PEMW algorithm, clustered according to one of the coefficient θ_{i_j}: (a) b_1, (b) b_2, (c) b_3, and (d) a_i. The AMSU/B FOVs are represented as uniform circles along the scan line.

[20] 3. Selection of the scenario such that the corresponding rr_1^*, rr_2^*, rr_3^* are strictly positive and at a minimum distance $dist^*$ between each other, i.e.:

$$\{rr_1^*, rr_2^*, rr_3^*\} = \arg \min_{k=1,\ldots,s} DIST(rr_{1_k}, rr_{2_k}, rr_{3_k}), \quad (3)$$

$$dist^* = DIST(rr_1^*, rr_2^*, rr_3^*) \quad (4)$$

and

$$rr_1^*, rr_2^*, rr_3^* > 0. \quad (5)$$

[21] 4. Estimation of the average rate rr_{av}^* between the three rain rates rr_1^*, rr_2^*, rr_3^* selected in the previous step.

Table 1. List of Case Studies for the Validation of the PEMW Algorithm Against the NIMROD Radar Observations

Case	Date	Radar Measurement (UTC)	Satellite Overpass (UTC)
1	7 July 2004	03:00	03:03
2	17 August 2004	13:30	13:29
3	25 June 2007	16:15	16:19
4	20 July 2007	15:15	15:15
5	2 July 2008	21:00	20:56
6	15 March 2008	16:15	16:20

Table 2. Contingency Table for the Dichotomous Statistical Assessment of the PEMW Algorithm on All Case Studies

PEMW Rain Detection	NIMROD Rain Detection	PEMW Performance	All Case Studies
Yes	yes	hits	2,218
Yes	no	false alarm	317
No	no	correct negatives	19,962
No	yes	misses	1,579

Table 3. Contingency Table for the Dichotomous Statistical Assessment of the PEMW Algorithm on the Individual Case Studies

PEMW Performance	Case 1	Case 2	Case 3	Case 4	Case 5	Case 6
Hits	231	273	399	369	339	507
False alarm	47	65	54	36	69	46
Correct negatives	3869	3274	2747	3662	3089	3321
Misses	129	162	382	198	256	452

Table 5. Dichotomous Statistics Results for All FOVs of the Individual Case Studies

Statistics	Case 1	Case 2	Case 3	Case 4	Case 5	Case 6
Accuracy	0.96	0.94	0.88	0.94	0.91	0.88
Bias score	0.77	0.82	0.66	0.71	0.68	0.58
POD	0.64	0.70	0.58	0.65	0.57	0.53
HSS	0.70	0.73	0.61	0.73	0.63	0.60
FAR	0.17	0.15	0.12	0.09	0.17	0.08

[22] 5. If the *dist** is less than a given threshold (depending on $rr*$), rr^*_{av} is the retrieved rain rate for the observed FOV, otherwise its value is set to zero.

[23] The above procedure is able to identify automatically the atmospheric scenario observed by the five radiometric channels, based on the assumption that given the real (or close to real) scenario and hence the coefficient associated with it, the regression curves corresponding to the three differences all retrieve similar rain rates. The three curves modeling the relationship between Δ_i and rr can be of a different type. Assuming they are all of the same type and more specifically linear, if the condition in step 5 of the PEMW algorithm is satisfied, the retrieved precipitation value is estimated as

$$rr^* = 1/3 \sum_{i=1,3} (a_{i_k} \Delta_i + b_{i_k}), \qquad (6)$$

where a_{i_k} and b_{i_k} for i = 1, 2, 3 are selected in step 3 of the algorithm among the s possible sextuples.

[24] The above algorithm is a specific version of a more general procedure which optimizes the distance between the three rr_1, rr_2, rr_3 in a continuous space of the parameters of the regression curves. Given the domains Λ_{i_j} of the coefficients θ_{i_j} of the curves $f(rr, \Delta_i | \theta_{i_1}, \ldots, \theta_{i_j}, \ldots, \theta_{i_c}) = 0$ for i = 1, 2, 3 and for j = 1, ..., c, the steps 2 and 3 of the above algorithm are substituted by the following optimization:

$$\{rr_1^*, rr_2^*, rr_3^*\} = \arg \min_{\Lambda_{1j}, \Lambda_{2j}, \Lambda_{3j}} DIST(rr_1, rr_2, rr_3), \qquad (7)$$

for j = 1, ..., c, such that:

$$f(rr_1, \Delta_1, \theta_{1_j}) = 0$$
$$f(rr_2, \Delta_2, \theta_{2_j}) = 0$$
$$f(rr_3, \Delta_3, \theta_{3_j}) = 0. \qquad (8)$$

3.3. Scenario Identification

[25] This section examines the regression coefficients selected by the PEMW algorithm in the case in which the retrieved rain rates are estimated as in equation (6). The coefficient table used in step 2 of the retrieval algorithm contains 3 discrete values for each b_i and 3 for each a_i, for i = 1, 2, 3. The table consists of 81 combinations of these

Table 4. Dichotomous Statistics Results for All Case Studies

Statistics	All FOVs	Radar rr $\geq$ 1 mm/h	Radar rr $\geq$ 5 mm/h
Accuracy	0.92	–	–
Bias score	0.67	–	–
POD	0.58	0.75	0.90
HSS	0.66	–	–
FAR	0.12	–	–

values, where b_1, b_2, b_3 vary independently while a_1, a_2, a_3 vary concomitantly from their minimum to maximum value. The reason of the latter is that the synthetic data show that the slope of the regression curves are related. Figure 3c illustrates the scenarios selected by the PEMW algorithm clustered according to the 3 values of the coefficient b_3 in a case study that will be considered also in the validation phase (section 4). In this case, as in all the others studied, b_3 clusters the scenarios giving rise to relatively wide homogeneous spatial areas. This verifies that neighboring FOVs show similarities in the identification of the scenarios. A similar behavior is observed when examining the selection of the values of b_2 (Figure 3b), while for b_1 the homogeneous areas are less wide (Figure 3a). The latter can be explained considering that the selection of b_1 is influenced also by ground emissivity (being Δ_1 the difference between the window channel observations) and hence measurements of neighbor FOVs are more diverse. The coefficients a_i, for i = 1, 2, 3, represent the slope of the regression curves and therefore tend to cluster the scenarios into three subsets according to the rainfall intensity, as is illustrated in Figure 3d.

[26] The above results are in agreement with the claim that each tuple of the regression coefficient table corresponds to a possible atmospheric/surface scenario, and that the retrieval procedure is able to select, for each FOV, the tuple corresponding to the scenario closest to the actual one.

4. Validation of the Rainfall Estimation Procedure

[27] The PEMW algorithm is validated in this section in a number of different ways: a comparison against radar products colocated within the AMSU/B FOVs, a FOV-to-point comparison against rain gauge measurements, a qual-
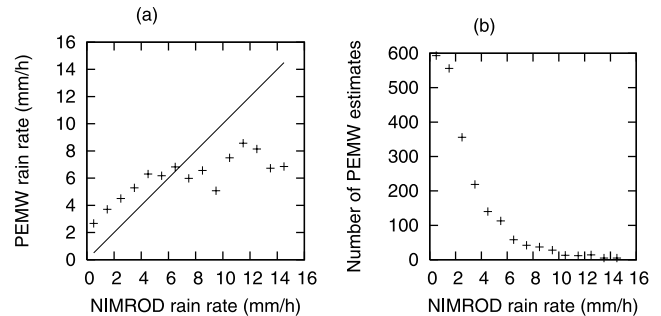

Figure 4. (a) Binned scatterplot: average PEMW rain rate estimates over 1 mm/h NIMROD rain rate bins. (b) Number of PEMW rain rate estimates in 1 mm/h NIMROD rain rate bins.

Table 6. Continuous Statistics Results

Statistics	Case 1	Case 2	Case 3	Case 4	Case 5	Case 6	All Cases
Me	2.19	2.07	−0.05	2.65	1.71	1.37	1.58
Mae	3.26	2.84	1.87	3.55	3.37	2.00	2.71
Rmse	4.18	3.73	2.65	4.63	4.25	2.67	3.65
Cc	0.18	0.48	0.10	0.35	0.35	0.49	0.38

itative comparison against a cloud optical thickness product, and a test over a snow covered surface. The settings of the algorithm are as follows and are valid for all the applications considered in this work. The PEMW estimates are obtained using linear regression curves and a table of coefficients a_{i_k} and b_{i_k} consisting of 81 sextuples. The function *DIST* is estimated as the sum of the three mutual differences between rr_{1_k}, rr_{2_k}, rr_{3_k}. The threshold used for *dist** in the step 5 of the algorithm is empirically set to 150% of rr^*_{av} for rr^*_{av} greater than 1 mm/h, and is set to 5 mm/h otherwise.

4.1. Comparison Against Radar Data

[28] The PEMW estimates are verified in a number of case studies of extreme events in the United Kingdom and neighboring countries. The list of rainy events considered in this study is reported in Table 1 together with the time of the satellite and radar observations. The time of the satellite observations is set to that of the satellite overpassing southeast England. Ground-based and satellite observations are at most 8 minutes apart in time, as the radar measurements are available every 15 minutes. As already stated in section 2.2, only AMSU/B FOVs which, according to the radar data, are full or clear of rain, and only radar rain rates less than 150 mm/h are taken into consideration in this study. The latter is done in order to minimize the errors in the radar data, while beam-filling issues are not the subject of the present study. The validation method is based on a number of different techniques [*Ebert*, 2008]:

[29] 1. Dichotomous statistical assessment (for verifying the accuracy of rain detection).

[30] 2. Continuous statistical assessment (for verifying the accuracy of rain estimation).

[31] 3. Qualitative assessment (for verifying the overall performance of the product).

[32] For the first two types of comparisons radar data are spatially averaged to the AMSU/B resolution. For this purpose, the area of each AMSU/B FOV is calculated using the ellipse axes provided by *Bennartz* [2000] for the different satellite viewing angles.

4.1.1. Dichotomous Statistical Assessment

[33] The dichotomous statistical assessment is a quantitative verification method; it is based on a number of statistics calculated from the contingency table reported in Table 2. The last column of the contingency table contains the detection results of the case studies listed in Table 1, while Table 3 shows the detection results relative to each single case study.

[34] The dichotomous statistics are reported in Table 4 for all FOVs considered in the case studies, and separately for the subset in which only relatively high rain rates are considered. Table 4 includes the accuracy, the bias score, the probability of detection (POD), the Heidke skill score (HSS) and the false alarm ratio (FAR) [*Ebert*, 2008]. The accuracy score shows that a big fraction (92%) of the FOVs are correctly identified as rainy or not rainy. Nevertheless, this result has to be seen in the right perspective as it is heavily influenced by the high occurrence of not rainy FOVs. The fraction of correctly identified FOVs after eliminating those which would be correct due to random chance (i.e., the HHS) gets down to 66%. The bias score indicates that the PEMW algorithm has a tendency to underestimate the area of a rain event (bias score <1), still does not tell how well the detected rain FOVs compare to the radar-derived rain FOVs. The POD score instead shows that 58% of the rain area is detected rightly, while 12% of the area detected as rainy is a false alarm (FAR). The
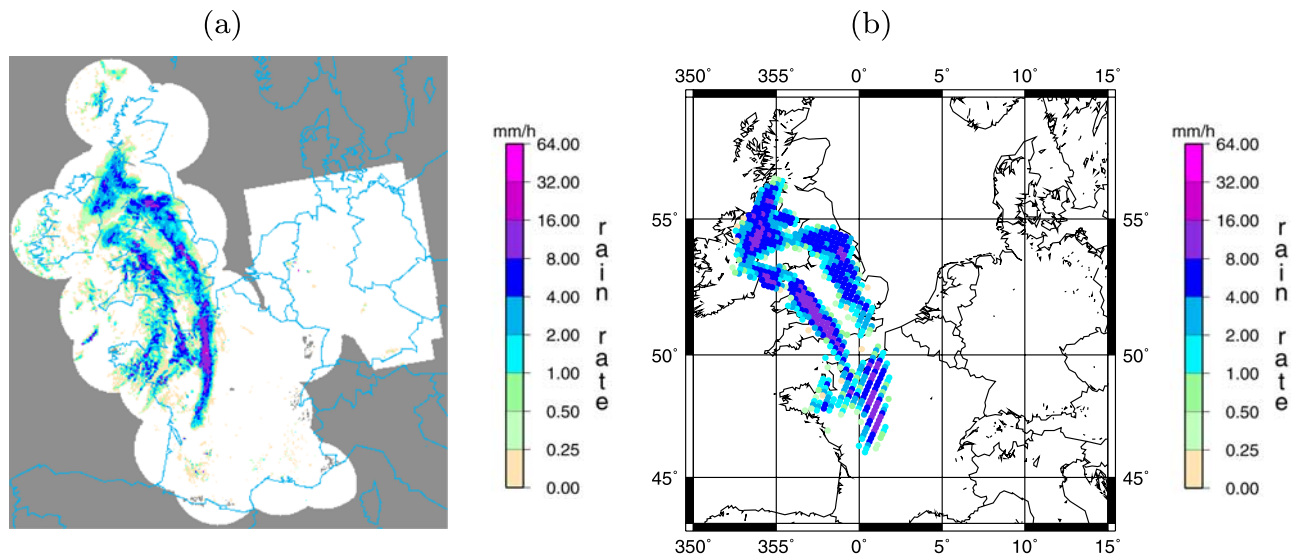
(a)

(b)

Figure 5. (a) NIMROD rain rate estimates at 08:00 UTC at full resolution and (b) PEMW rain rate retrieval at 07:55 UTC on 8 January 2004. The AMSU/B FOVs are represented as uniform circles along the scan line.
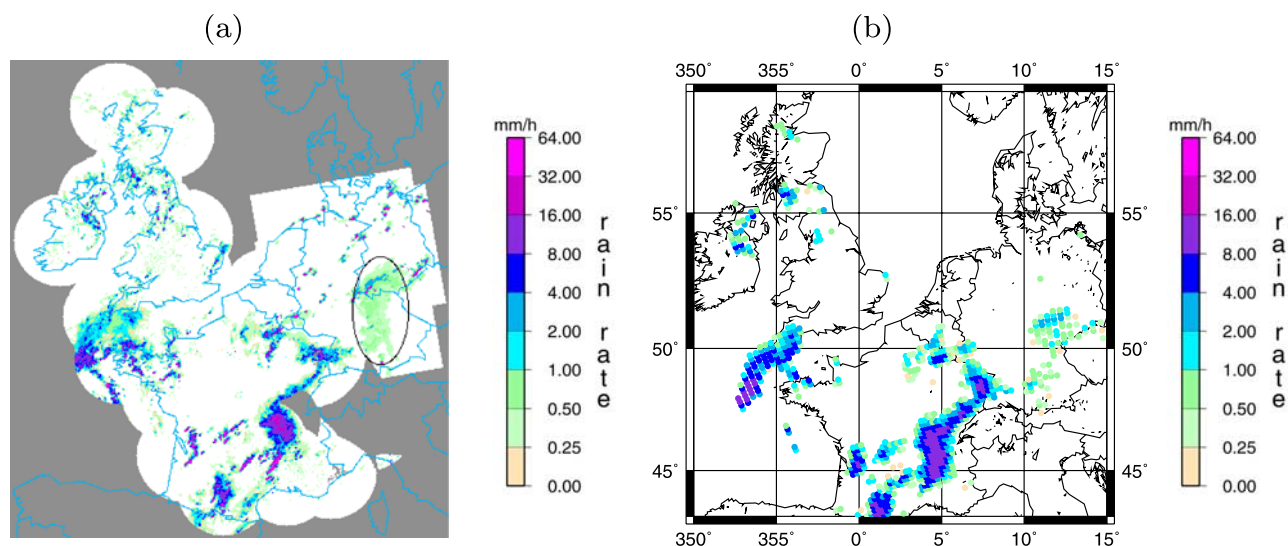
Figure 6. (a) NIMROD rain rate estimates at 13:30 UTC at full resolution and (b) PEMW rain rate retrieval at 13:29 UTC on 17 August 2004. The AMSU/B FOVs are represented as uniform circles along the scan line.

probability of detection increases to 75% and to 90% when radar rain rates are greater than 1 mm/h and 5 mm/h, respectively. This is a positive result in particular when considering extreme events. The results from the individual case studies, reported in Table 5, show a relatively small variability.

[35] The above results conducted over a small set of case studies show PEMW algorithm considerable ability to discriminate rain from no rain.

4.1.2. Continuous Statistical Assessment

[36] The continuous statistical assessment is a quantitative verification method which validates the accuracy of rain rate estimation. The scatter analysis for the FOVs in the hit set is performed following the approach in *Ferraro and*

Marks [1995]: the radar data are binned in 1 mm/h rain rate intervals and the satellite estimates in these bins are averaged. The binned scatterplot shows a reasonably good correlation between AMSU/B and NIMROD estimates, but with AMSU/B overestimating light rain, and conversely, underestimating heavy rain (see Figure 4a). The above binned analysis is performed in order to place equal emphasis on the entire range of rain rates as well as to minimize match-up errors between ground and satellite observations. It should be noted that the results at higher rain rates become less reliable as the number of FOVs within a bin decreases (see Figure 4b). In particular, beyond 15 mm/h the number of FOVS in a bin is less than 5. For this reason, the continuous statistics are estimated for rain
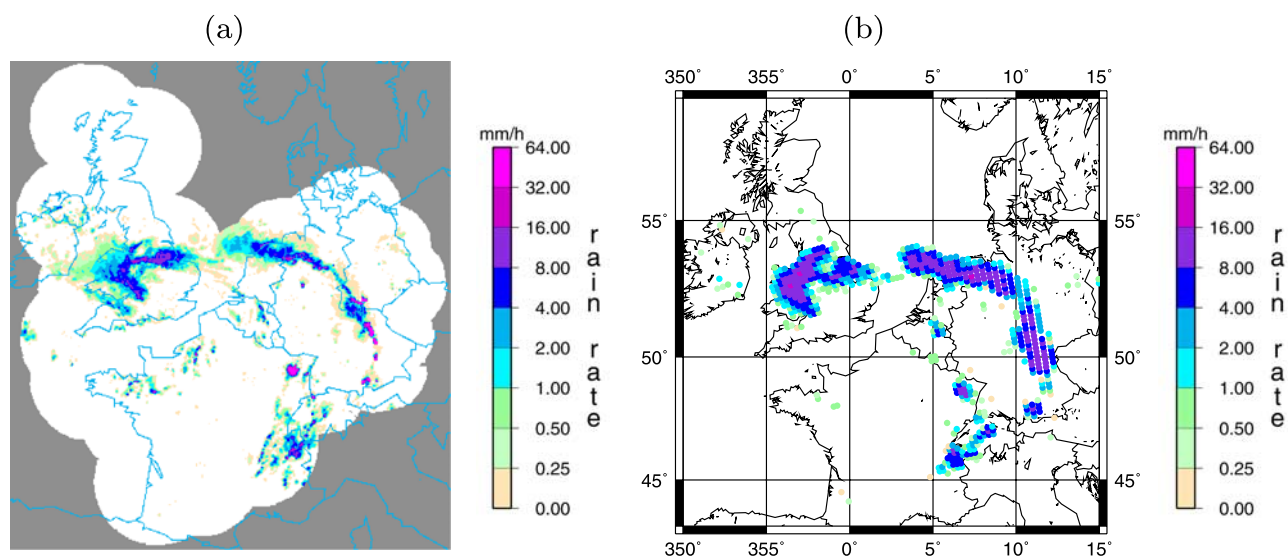

Figure 7. (a) NIMROD rain rate estimates at 15:15 UTC at full resolution and (b) PEMW rain rate retrieval at 15:15 UTC on 20 July 2007. The AMSU/B FOVs are represented as uniform circles along the scan line.
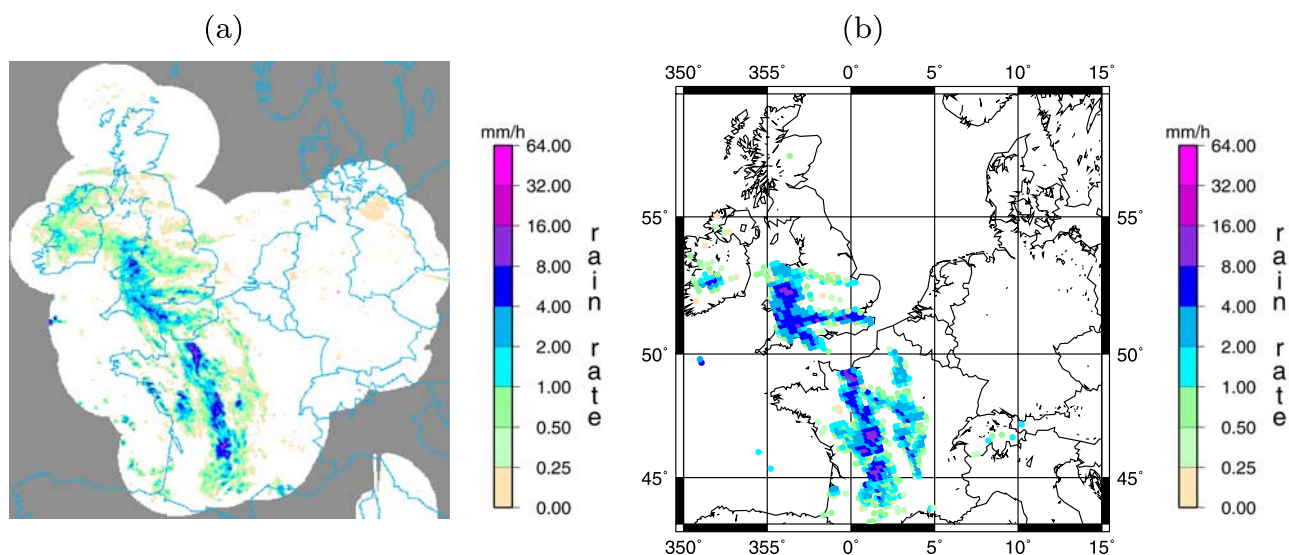
Figure 8. (a) NIMROD rain rate estimates at 16:15 UTC at full resolution and (b) PEMW rain rate retrieval at 16:20 UTC on 15 March 2008. The AMSU/B FOVs are represented as uniform circles along the scan line.

rate values in the hit set up to 15 mm/h (neglecting only 1.5% of the data). The mean error (me), the mean absolute error (mae), the root-mean squared error (rmse) and the correlation coefficient (cc) for a linear fit are reported in Table 6 for the individual cases and for all case studies, and show that the PEMW algorithm has some ability to estimate rain rates. In particular when considering all case studies, the cc is 0.38 and the rmse is 3.65. The algorithm performs better in some cases than in others in a way that might depend on the type of event. In particular, the case study number 3, having the worst cc, is relative to a consistent number of narrow rain areas which are small compared to the wide AMSU/B FOVs.

4.1.3. Qualitative Assessment

[37] Four individual cases are considered here for eye-balling assessment, that is a qualitative type of assessment which, despite being potentially biased, can provide an immediate initial perception of the retrieval quality. The rain rate retrieved by the NIMROD radar network are visually compared, at a full resolution, to the rain rate estimated by PEMW for the case of 8 January 2004 in Figure 5, 17 August 2004 in Figure 6, 20 July 2007 in Figure 7, and 15 March 2008 in Figure 8. For easier comparison the same rain rate scale is used in all the figures. The above case studies indicate a very good agreement between the AMSU/B algorithm and NIMROD in the detection of rain.

[38] Figure 6 shows that the PEMW algorithm is able to retrieve an area of light rain (enclosed in the oval line in the figure), while Figure 9 illustrates that the convective index classification used in the NESDIS algorithm [*NESDIS/NOAA*, 2008], when applied to the PEMW-derived rainy FOVs of the case study in Figure 6, is not able to classify the above light rain area. This case study shows the usefulness of using the additional window channels for their ability to sense low-level precipitation. In fact, the convective index classification uses only the three AMSU/B opaque channel observations to discriminate precipitation

systems. For the same case study the values used in the estimation of the above dichotomous and continuous statistics are reported in Figure 10: the radar data resampled over the AMBU/B FOVS (a), and the corresponding PEMW retrieval (b). Figure 11 shows the difference values (NIMROD estimates minus PEMW estimates) for the same event.

4.2. Comparison Against Rain Gauge Measurements

[39] The PEMW algorithm is tested against the Surface Meteorology Station (SMET) rain gauge observations at Nauru. The results are provided as a qualitative type of assessment with a FOV-to-point comparison. Nauru is a
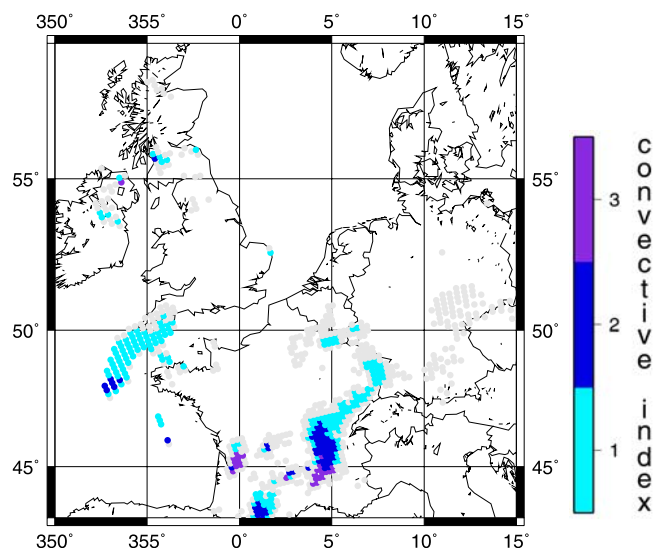

Figure 9. Classification of PEMW-derived rainy FOVs according to the convective index definition for the case of 17 August 2004 at 13:29 UTC. The gray pixels are the ones not classified. The AMSU/B FOVs are represented as uniform circles along the scan line.
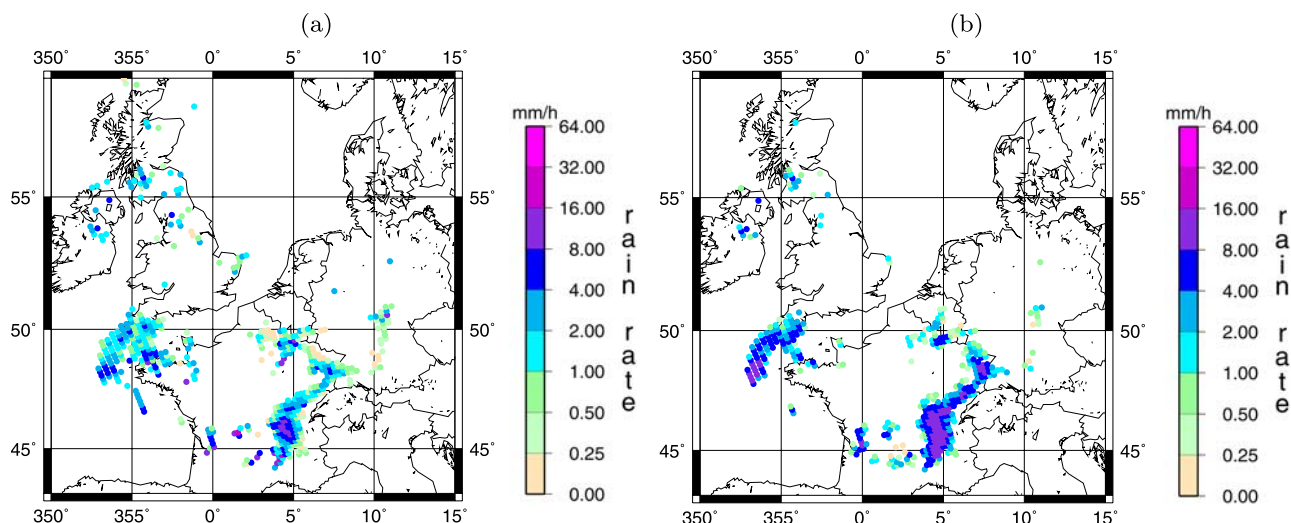
Figure 10. (a) NIMROD rain rate estimates at 13:30 UTC resampled to AMSU/B resolution and (b) PEMW rain rate retrieval at 13:29 UTC on 17 August 2004. The AMSU/B FOVs are represented as uniform circles along the scan line.

21 km^2 island; hence, the AMSU/B observations in proximity of the island cover a surface which is mostly water (less than one twelfth of AMSU/B FOV at nadir is covered by land). Figure 12 illustrates how the AMSU/B rain retrieval compares with the SMET rain gauge observations on a number of case studies. The rain gauge observations are drawn up to 30 mm/h in order to optimize the quality of the figure. The AMSU/B algorithm estimates exhibit a good agreement with the rain gauge observations both for rain and no rain events.

[40] An additional comparison is made in Figure 13 between the Moderate Resolution Imaging Spectroradiometer (MODIS) cloud optical thickness product [*LAADS Web/ NASA*, 2008] at 22:50 UTC (a) and the PEMW retrieval at 23:06 UTC (b) for the case of 30 January 2007 of Figure 12. The detected rain area matches very well the area covered by thick clouds. The arrow in the figure indicates the location of the Nauru Island and shows that the AMSU/B FOV over the island appears to be fully overcast by thick clouds. This might explain a retrieval value of 13.4 mm/h by the PEMW algorithm against a point value of 4.6 mm/h (the average measurement in the time interval 23:01 to 23:11 UTC) by the ARM rain gauge.

4.3. Snow on the Ground

[41] A further individual case is illustrated here to show how snow surfaces do not affect the rainfall retrieval by the PEMW algorithm. Brightness temperature depression due to snow on the ground, evident mainly in the window channel observations, could mistakenly be attributed to rainfall. The threshold used in step 5 of the algorithm together with the requirement in step 3 of rr_i to be strictly positive, allows for snow on the ground not to be detected as rainfall. This can be explained considering that the cold depression due to snow surface is much stronger in the window than in the opaque channel observations. Figure 14 illustrates the retrieval over the Alps region on 7 February 2008, a day with clear sky. It can be clearly seen that numerous FOVs on the Alps region are wrongly detected as precipitating

when no constraints are used (Figure 14a), while the number of false alarms is reduced considerably when they are used (Figure 14b). This case study shows the usefulness of using the additional opaque channels as they are less affected by ground emissivity. The related problem of detecting rainfall over snow covered surfaces is instead the subject of ongoing work.

5. Summary and Conclusions

[42] The PEMW algorithm exploits the peculiar sensitivity of the AMSU/B channels, both window and opaque, to different rainy situations, which depends on parameters like the altitude and size of precipitation particles, as well as on
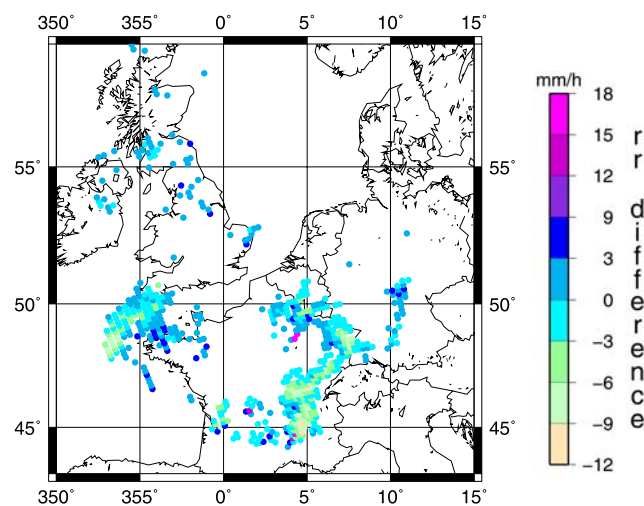

Figure 11. Difference between NIMROD rain rate estimates at 13:30 UTC resampled to AMSU/B resolution and PEMW rain rate retrieval at 13:29 UTC on 17 August 2004. The AMSU/B FOVs are represented as uniform circles along the scan line.
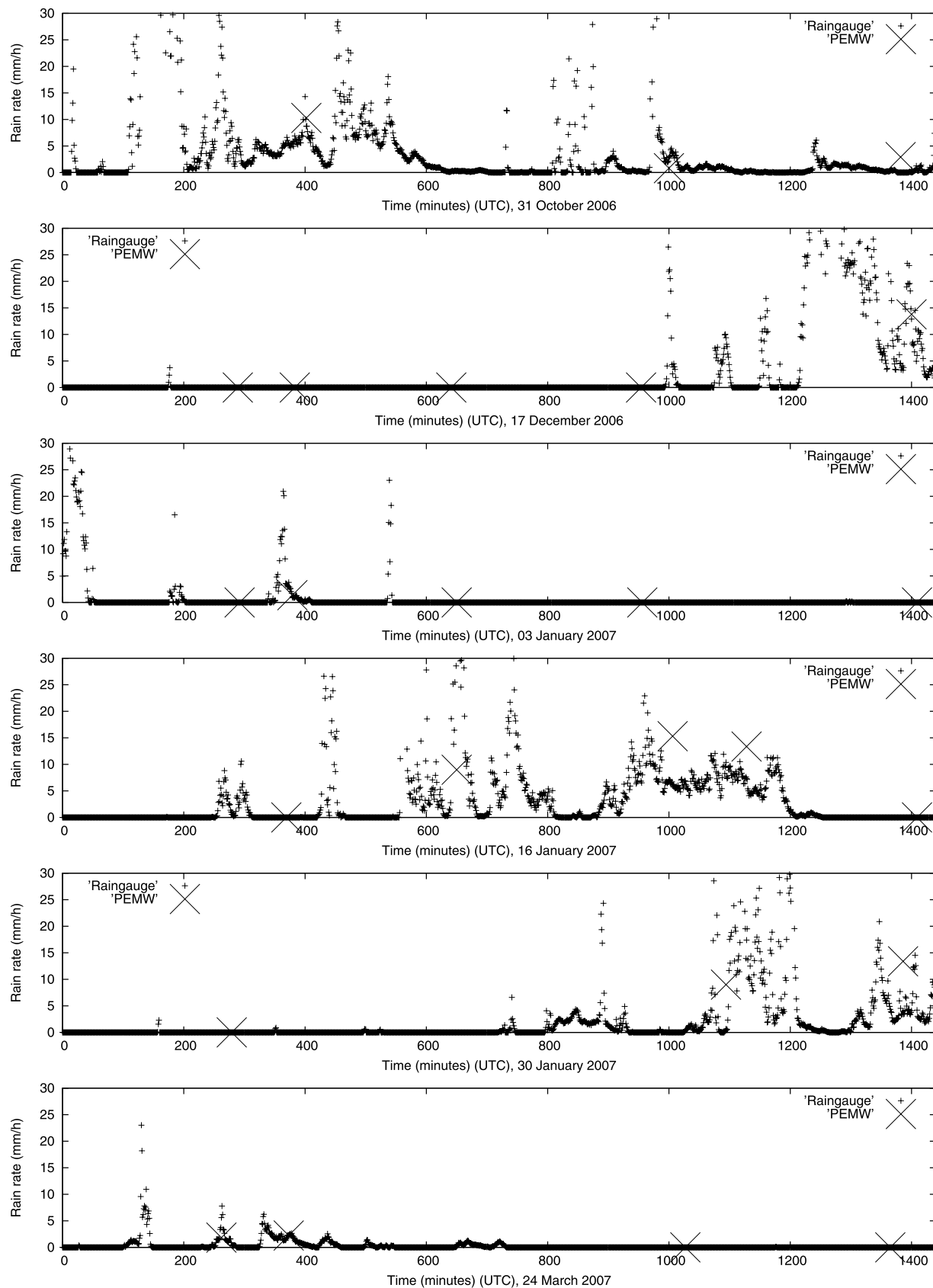
Figure 12. ARM rain gauge observations and PEMW rain rate retrieval on a number of overpasses of NOAA satellites over Nauru Island.
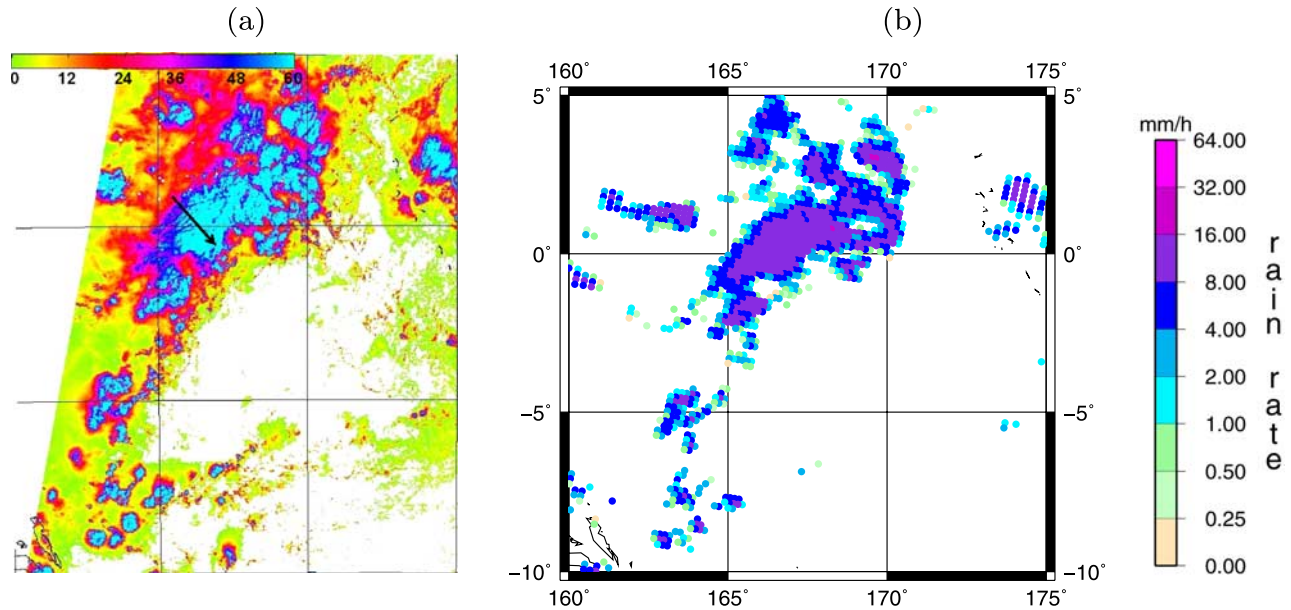
Figure 13. (a) MODIS cloud optical thickness at 22:50 UTC and (b) PEMW rain rate retrieval at 23:06 UTC on 30 January 2007. The AMSU/B FOVs are represented as uniform circles along the scan line.

the atmospheric profiles. The window channels have been exploited for their ability to detect the scattering signal of precipitation-sized ice particles, which is indirectly related to precipitation rate. They have been utilized for this reason in various previous techniques, among them the NESDIS operational rain rate algorithm. Furthermore, the two window channels can sense low-level precipitation which could be missed by the high frequency opaque channels and that could occur for example, in tropical regions. On the other hand, microwave measurements in window channels are strongly affected by surface emissivity which is difficult to estimate because it is a function of several varying parameters like surface moisture and roughness. AMSU/B

opaque channels are not only less affected by ground emissivity but they can sense precipitation through detecting the cold signature caused by the hydrometeor scattering. At these frequencies the scattering effect is also strong in the absorption band. The peculiarity of the three opaque channels is to sound different altitudes because of their different frequency bands around 183 GHz. The channel at 183 ± 1 GHz senses high convective systems, while the ones at 183 ± 3 GHz and at 183 ± 7 GHz can sense also low- and middle-altitude precipitation. The higher channels are particularly useful in cases in which the channel at 183 ± 7 GHz reaches the surface because of very dry atmospheric conditions.
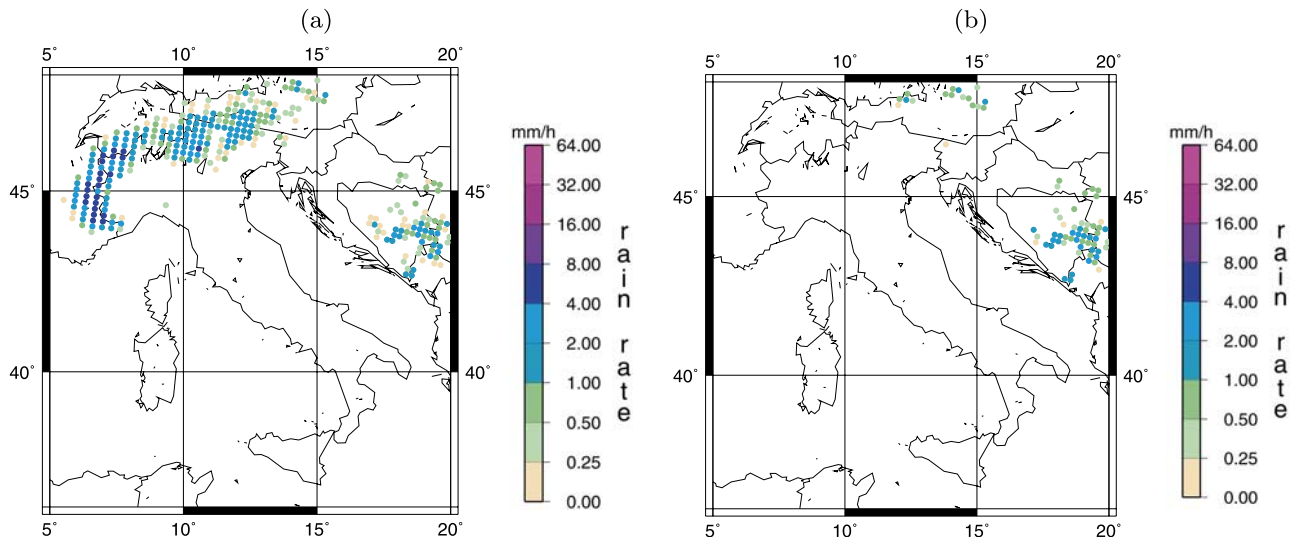

Figure 14. PEMW rain rate retrieval on 7 February 2008 at 04:49 UTC (a) when constraints are not used and (b) when they are used. In the latter case the number of false alarms is reduced considerably. The AMSU/B FOVs are represented as uniform circles along the scan line.

[43] The PEMW algorithm takes into account all the above physical properties, through an extensive set of regression curves between brightness temperature differences and rain rates under various atmospheric and surface conditions. The brightness temperature differences are informative as the channels respond differently in the presence of precipitation than in clear scenes. The algorithm is based entirely on AMSU/B observations and gives an estimate of rainfall such that every channel agrees on it according to the possible physical responses to precipitation. Here lies the peculiarity and novelty of the algorithm and the reason of its success, as is shown in the verification section.

[44] The PEMW algorithm has been validated on a number of case studies at middle and low latitudes, and over land and land/water surfaces. The algorithm estimates exhibit a very good agreement with ground-based (both radar and rain gauge) observations in the detection of rainfall and with the MODIS cloud optical thickness product. The probability of detection of precipitation is 75% and 90% for rain rates greater than 1 mm/h and 5 mm/h, respectively. Considering the fact that it is difficult to know the exact true amount of precipitation, the algorithm provides also a reasonably good estimation of rain rate values. In fact, both radar and rain gauges are prone to errors which has to be taken into account in any comparison between satellite and ground-based derived products. Furthermore, due to the use of both window and opaque channels, it has been shown that the algorithm is able to retrieve light rain and not to misidentify snow-covered surfaces as rain.

References

Bennartz, R. (2000), Optimal convolution of AMSU-B to AMSU-A, *J. Atmos. Oceanic Technol.*, *17*, 1215–1225.

Bennartz, R., A. Thoss, A. Dybbroe, and D. B. Michelson (2002), Precipitation analysis using the Advanced Microwave Sounding Unit in support of nowcasting applications, *Meteorol. Appl.*, *9*, 177–189.

Chen, F. W., and D. H. Staelin (2003), AIRS/AMSU/HSB precipitation estimates, *IEEE Trans. Geosci. Remote Sens.*, *41*, 410–417.

Ebert, E. (2008), Forecast Verification — Issues, Methods and FAQ, 5 Dec. (Available at http://www.bom.gov.au/bmrc/wefor/staff/eee/verif/verif_web_page.html)

Ferraro, R., and G. F. Marks (1995), The development of SSM/I rain-rate retrieval algorithms using ground-based radar measurements, *J. Atmos. Oceanic Technol.*, *12*, 755–770.

Ferraro, R., F. Weng, N. C. Grody, L. Zhao, H. Meng, C. Kongoli, P. Pellegrino, S. Qiu, and C. Dean (2005), NOAA operational hydrological products derived from the Advanced Microwave Sounding Unit, *IEEE Trans. Geosci. Remote Sens.*, *43*, 1036–1049.

Grody, N. C. (1991), Classification of snow cover and precipitation using the Special Sensor Microwave Imager, *J. Geophys. Res.*, *96*(D4), 7423–7435.

Joyce, R. J., J. E. Janowiak, P. A. Arkin, and P. Xie (2004), CMORPH: A method that produces global precipitation estimates from passive microwave and infrared data at high spatial and temporal resolution, *J. Hydrometeorol.*, *5*, 487–503.

Kongoli, C., P. Pellegrino, R. R. Ferraro, N. C. Grody, and H. Meng (2003), A new snowfall detection algorithm over land using measurements from the Advanced Microwave Sounding Unit (AMSU), *Geophys. Res. Lett.*, *30*(14), 1756, doi:10.1029/2003GL017177.

Kummerow, C., et al. (2001), The evolution of the Goddard Profiling Algorithm (GPROF) for rainfall estimation from passive microwave sensors, *J. Appl. Meteorol.*, *40*, 1801–1820.

LAADS Web/NASA (2008), Level 1 and Atmosphere Archive and Distribution System, 5 Dec. (Available at http://ladsweb.nascom.nasa.gov)

NCDC/NOAA (2008), NOAA KLM User's Guide Section 3.4, 5 Dec. (Available at http://www2.ncdc.noaa.gov/docs/klm/html/c3/sec3-4.htm)

NESDIS/NOAA (2008), Microwave Surface and Precipitation Products System (MSPPS) Algorithms, 5 Dec. (Available at http://www.star.nesdis.noaa.gov/corp/scsb/mspps/algorithms.html)

Qiu, S., P. Pellegrino, R. Ferraro, and L. Zhao (2005), The improved AMSU rain-rate algorithm and its evaluation for a cool season event in the western United States, *Weather Forecast.*, *20*, 761–774.

Rico-Ramirez, M. A., I. D. Cluckie, G. Shepherd, and A. Pallot (2007), A high-resolution radar experiment on the island of Jersey, *Meteorol. Appl.*, *14*, 117–129.

Rosenkranz, P. W. (2002), Radiative transfer solution using initial values in a scattering and absorbing atmosphere with surface reflection, *IEEE Trans. Geosci. Remote Sens.*, *40*, 1889–1892.

Staelin, D. H., and F. W. Chen (2000), Precipitation observations near 54 and 183 GHz using the NOAA-15 satellite, *IEEE Trans. Geosci. Remote Sens.*, *38*(5), 2322–2332.

UK Met Office (2008a), Met Office: NWP SAF, ATOVS and AVHRR Pre-processing Package (AAPP), 5 Dec. (Available at http://www.metoffice.gov.uk/research/interproj/nwpsaf/aapp/index.html)

UK Met Office (2008b), Rain Radar Products (NIMROD), British Atmospheric Data Centre, 2003, 5 Dec. (Available at http://badc.nerc.ac.uk/data/nimrod)

UK Met Office (2008c), Met Office: NWP SAF, RTTOV Radiative Transfer Model and Profile Datasets, 5 Dec. (Available at http://www.metoffice.gov.uk/research/interproj/nwpsaf/rtm/index.html)

Vila, D., R. Ferraro, and R. Joyce (2007), Evaluation and improvement of AMSU precipitation retrievals, *J. Geophys. Res.*, *112*, D20119, doi:10.1029/2007JD008617.

―――――――――――――

V. Cuomo, E. Di Tomaso, and F. Romano, Istituto di Metodologie per l'Analisi Ambientale, Consiglio Nazionale delle Ricerche, C. da S. Loja, I-85050 Tito Scalo (PZ), Italy. (cuomo@imaa.cnr.it; ditomaso@imaa.cnr.it; romano@imaa.cnr.it)